Interacting synapses stabilise both learning and neuronal dynamics in biological networks

Everton J. Agnes[1,2,*] and **Tim P. Vogels**[1,3]

[1]*Centre for Neural Circuits and Behaviour, University of Oxford, OX1 3SR Oxford, United Kingdom*
[2]*Biozentrum, University of Basel, 4056 Basel, Switzerland*
[3]*Institute of Science and Technology Austria, 3400 Klosterneuburg, Austria*

Distinct synapses influence one another when they undergo changes, with unclear consequences for neuronal dynamics and function. Here we show that synapses can interact such that excitatory currents are naturally normalised and balanced by inhibitory inputs. This happens when classical spike-timing dependent synaptic plasticity rules are extended by additional mechanisms that incorporate the influence of neighbouring synaptic currents and regulate the amplitude of their efficacy changes accordingly. The resulting control of excitatory plasticity by inhibitory activation, and vice versa, gives rise to quick and long-lasting memories as seen experimentally in receptive field plasticity paradigms. In models with additional dendritic structure, we observe experimentally reported clustering of co-active synapses that depends on initial connectivity and morphology. Finally, in recurrent neuronal networks, rich and stable dynamics with high input sensitivity emerge, providing transient activity that resembles recordings from motor cortex. Our model provides a general framework for codependent plasticity that frames individual synaptic modifications in the context of population-wide changes, allowing us to connect micro-level physiology with network-wide phenomena.

The remarkable property of synapses to change – synaptic plasticity – is hypothesised to be the brain's fundamental learning mechanism, and it has generated a large body of theoretical and experimental work[1–3]. Based on Hebb's postulate and early experimental data, theories have focused on the idea that synapses change depending on the activity of its pre- and postsynaptic counterparts, constituting a strong locality constraint. However, experimental evidence[4–11] has pointed towards learning mechanisms that also act non-locally, taking into account the activity at multiple synapses and even network state, for both excitatory and inhibitory synapses.

Excitatory synaptic plasticity (ESP) has long been known to rely on intersynaptic cooperativity by way of elevated calcium concentrations from the activation of multiple presynaptic excitatory synapses[8–11]. Interestingly, GABAergic, inhibitory synaptic plasticity (ISP) has also been shown to depend on the activation of neighbouring excitatory synapses[4,5] and on the ratio of local excitatory and inhibitory currents (EI balance)[4]. Finally, inhibitory currents can affect ESP by flipping the direction of efficacy changes according to the absence or presence of inhibitory currents in the vicinity of the synapse[6,7]. Long-term potentiation (LTP) at excitatory synapses has also been shown to depend on the distance and timing between successive LTP induction of neighbouring excitatory synapses[12]. Based on this experimental evidence we introduce a novel model of *codependent* synaptic plasticity, which takes into account the direct interaction between different synapses during plasticity. Our model reproduces a wide range of experimental data on excitatory plasticity, receptive field plasticity of excitatory and inhibitory synapses, synaptic clustering based on morphology, and stabilisation of amplified dynamics in recurrent networks.

In our framework (Fig. 1A), a synapse changes according to a function $\phi(E, I; \text{PRE}, \text{POST})$, in which E and I describe the recent postsynaptic activation of nearby excitatory and inhibitory synapses, respectively. The activity of the synapse's own pre- and postsynaptic neurons are described by PRE and POST. We consider E and I to be variables that depend on input currents: calcium influx through N-methyl-D-aspartate (NMDA) channels for E, and chloride influx through γ-Aminobutyric acid type A (GABA_A) channels for I (see Supplementary Material; Supp. M.). At excitatory synapses, $\phi(E, I; \text{PRE}, \text{POST})$ changes synaptic efficacy similarly to classic Hebbian spike-timing dependent plasticity (STDP)[8,13] (Fig. 1Bi), but in addition, neighbouring excitatory activity modulates synaptic changes in accordance with experimental results. Specifically, the learning rate for the Hebbian-LTP term increases linearly with neighbouring excitatory inputs[8,9,11] while heterosynaptic plasticity decreases synaptic efficacies via a quadratic dependency on the excitatory inputs[14] (Fig. 1Bii), counterbalancing the potentially de-stabilising positive feedback from Hebbian-LTP. Elevated inhibitory activity blocks excitatory plasticity[15], but allows for quick learning when the system undergoes disinhibition (Fig. 1Biii). Inhibitory synapses change according to a symmetric STDP curve[4,16] (Fig. 1Ci), but their learning-rate is modulated by the ratio of neighbouring excitatory and inhibitory activity (Fig. 1Cii,Ciii), such that when E and I currents are equal ($E = I$), or $E = 0$[4,5], there is no change in efficacy.

We tested the interplay between spike times and input currents through $\phi(E, I; \text{PRE}, \text{POST})$ in a leaky integrate-and-fire (LIF) neuron with plastic excitatory (AMPA and NMDA) synapses, as well as inhibitory (GABA_A) synapses (Supp. M.). We were able to capture many excitatory plasticity features, e.g., dependency on both the membrane potential depolarisation (Fig. 1D, left) and the frequency of pre- and postsynaptic spike pairs (Fig. 1D, right). In our model, high-frequency of pre- and postsynaptic spike pairs elicited increased LTP due to a direct elevation in NMDA currents, unlike spike-[19] or voltage-based[20] models that emulate this effect by detecting an increase in the postsynaptic firing frequency (Supp. M.). The explicit regulation of plasticity via excitatory and inhibitory currents highlights the different roles of excitation and inhibition for plasticity, which are inseparable in typical spike- or voltage-based learning rules (Fig. S1). Additionally, the positive feedback mechanism of Hebbian-LTP[17,21] is controlled by intrinsic heterosynaptic plasticity, creating a stable set-point for the excitatory currents (Fig. 1Bii, red circle). This set-point is determined by the ratio between heterosynaptic plasticity and Hebbian-LTP, independently of initial excitatory weights and inhibitory input strength (Fig. 1E). It acts as a normalisation

* Correspondence: everton.agnes@gmail.com;

1st April 2021

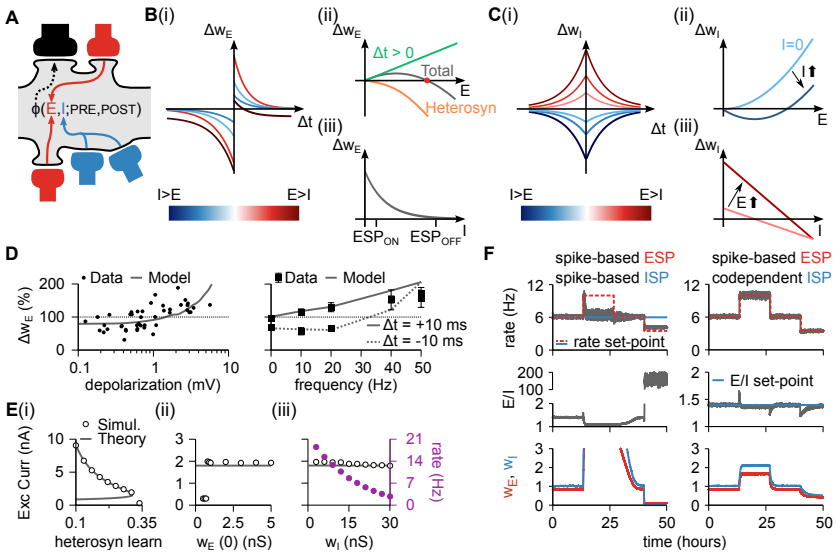

FIG. 1. Codependent synaptic plasticity normalises excitatory input and balances EI inputs. **A**, Plasticity of a synapse (black) depends on the activation of neighbouring excitatory (red) and inhibitory (blue) synapses. **B**, Codependent excitatory plasticity. (*i*), Excitatory weight change, Δw_E, is a function of the time interval between post and presynaptic spikes, Δt, and neighbouring synaptic inputs, E and I. (*ii*) Excitatory inputs, E, control Hebbian-LTP ($\Delta t > 0$) and heterosynaptic plasticity, creating a common fixed point for the total excitatory input (red dot). (*iii*), Inhibitory inputs, I, gate excitatory plasticity ('ON' *vs* 'OFF'). **C**, Codependent inhibitory plasticity. Inhibitory weight change, Δw_I, is a function of Δt (*i*), E (*Cii*) and I (*Ciii*) as in B. **D**, Fit of STDP experiments in mouse visual cortex for codependent excitatory plasticity, capturing observed voltage dependency[9] (left) and frequency dependency[8] (right) of synaptic changes. **E**, Total excitatory input (after learning) as a function of the ratio of the heterosynapic learning rate (*i*), initial excitatory weight (*ii*), and inhibitory weight (*iii*); inhibitory strength controls the postsynaptic neuron's firing-rate (*iii*; purple). **F**, Firing-rate (top), ratio between excitatory and inhibitory inputs (middle), and input weights normalised to initial value (bottom). Combination of excitatory[17] and inhibitory[18] spike-based rules (left); excitatory spike-based[17] and codependent inhibitory synaptic learning rules (right). Lines in the top panel indicate firing-rate fixed-points from excitatory (red) and inhibitory (blue) learning rules.

mechanism of excitatory inputs, resembling homeostatic regulation of excitatory bouton size in dendrites[22]. Importantly, inhibitory plasticity balances excitatory and inhibitory currents without imposing a firing-rate set-point, avoiding competition with excitatory plasticity (Fig. 1F).

To assess the functional consequence of codependent plasticity, we studied its performance in receptive fields formation for both excitatory and inhibitory synapses jointly[23]. We simulated a postsynaptic LIF neuron receiving inputs from 8 pathways (Supp. M.) that represent, e.g., different sound frequencies[18,23] (Fig. 2A). In this scenario, inhibitory activity acted as a gating mechanism for excitatory plasticity, by keeping the learning rate at a minimum when inhibitory currents were high (Fig. 1Biii). Excitatory input weights could thus only be changed during periods of presynaptic disinhibition, i.e., the learning window (Fig. S2), and were otherwise stable[23] (Fig. 2B,C; see Fig. S3 for when gating is weak). Inhibitory weights, due to the spike-timing dependence of codependent ISP, precisely mirrored the excitatory receptive field after the learning window (Fig. 2D), a phenomenon known as detailed balance[3]. Changes in both excitatory and inhibitory inputs due to codependent plasticity robustly reproduced experimental results in rat auditory cortex[23] (Fig. 2E) without additional fine tuning.

Next, we attached passive dendritic compartments to the soma of our model to assess how our learning rules affected the dendritic organisation of synapses. Due to their largely passive properties, the membrane potential of dendrites could be depolarised to values above the somatic spiking threshold depending on their proximity, i.e., electrotonic distance, to the soma (Fig. 3A). Super-threshold membrane potential fluctuations gave rise to larger NMDA and $GABA_A$ current fluctuations in distal dendrites (Fig. 3B). When excitation and inhibition were unbalanced (i.e., when receiving uncorrelated inputs), distal dendrites could undergo fast changes due to the current-induced high learning rates for excitatory plasticity (Fig. 3B, thick red line). However, when currents were balanced (i.e., when receiving correlated excitatory and inhibitory inputs), large inhibitory currents gated excitatory plasticity off despite strong excitation, effectively blocking excitatory plasticity in these compartments (Fig. 3B, thick blue line). Additionally, the larger distance to the soma, and its consequently weaker passive coupling (Fig. 3C), meant that distal dendrites had smaller influence on the initiation of postsynaptic spikes.

As a consequence of these two effects – location dependent learning-rates and influence on spike initiation – synapses developed differently according to their somatic proximity (Fig. 3D), and according to the activity of their neighbouring inputs. When the majority of excitatory inputs onto a dendritic compartment were co-active (i.e., originated from the same source), co-active synapses were strengthened, creating a cluster of similarly tuned inputs onto a compartment. Independently active excitatory synapses weakened and eventually faded away (Fig. 3D, middle). In contrast, when more than a certain number of excitatory inputs were independent, co-active synapses decreased in weight and faded, while independently active excitatory synapses strengthened (Fig. 3D, right). The number of co-active excitatory synapses necessary for a dendritic compartment to develop single-feature tuning varied with somatic proximity, and whether excitation and inhibition were matched (Fig. 1E; see Fig. S4 for weight dynamics). Notably, in the balanced state, substantially more co-active excitatory synapses were necessary to create clusters for at distal than at proximal dendrites (Fig. 1E), because only large groups of co-active excitatory synapses could initiate (LTP-inducing) pre-before-post spike pairs. Thus, single-feature selectivity[25,26] or mixed selectivity[27] emerged in our model depending on the branch architecture of the dendritic host structure[28,29] (Fig. 3F).

Up to this point we explored the effects of codependent synaptic plasticity in a single postsynaptic neuron. However, the recurrent neuronal circuits typically amplify instabilities of any synaptic plasticity rules at play[17,21]. We thus investigated codependent plasticity in a recurrent neuronal network of 1250 spiking neurons (Supp. M.; Fig. 4A). In our model, excitatory and inhibitory codependent plasticity allowed the network to self-stabilise in a high-conductance state[30], with low effective neuronal membrane time-constants (Fig. 4C), and strong excitatory connections that were precisely balanced by equally strong inhibition (Fig. 4B and Fig. S5). Further, the network exhibited a wide distribution of baseline firing-rates (Fig. 4D), similar to what has been observed in cortical recordings *in vivo*[31]. We analysed the final connectivity matrix of the network

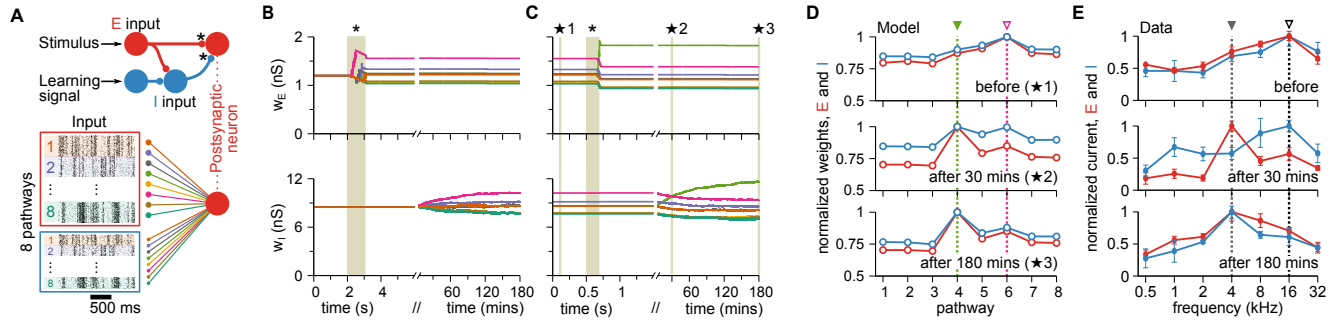

FIG. 2. Receptive field plasticity. **A**, External stimulus (e.g., sound) activates a set of correlated excitatory and inhibitory afferents (simulated as inhomogeneous Poisson point processes) that feed forward onto a postsynaptic neuron with plastic synapses (*). Eight group pathways, consisting of 100 excitatory and 25 inhibitory afferents each, have correlated spike trains. The responsiveness of inhibitory afferents can be modulated by an additional learning signal. **B**, Time course of excitatory (top) and inhibitory (bottom) weights (colour coded by groups). During a "learning window", indicated by the shaded area (*), all inhibitory afferents are down-regulated. The sequential activation of excitatory input groups (Fig. S2) in the absence of inhibition establishes a receptive field profile. **C**, Continued simulation from B. Weights are stable until inhibition is down-regulated for a 200-millisecond window (*), during which the green pathway (#4) is activated (Fig. S2). Consequently, the preferred input pathway switches from #6 (pink) to #4 (green). **D**, Snapshots of the average synaptic weights for the different pathways before (top), immediately after plasticity induction (middle), and at the end of the simulation as indicated by the ⋆ symbols in C. **E**, Experimental data[23] shows receptive field profiles of excitatory and inhibitory inputs before (top), as well as 30 minutes (middle) and 180 minutes (bottom) after pairing of non-preferred tone and nucleus basalis activation.

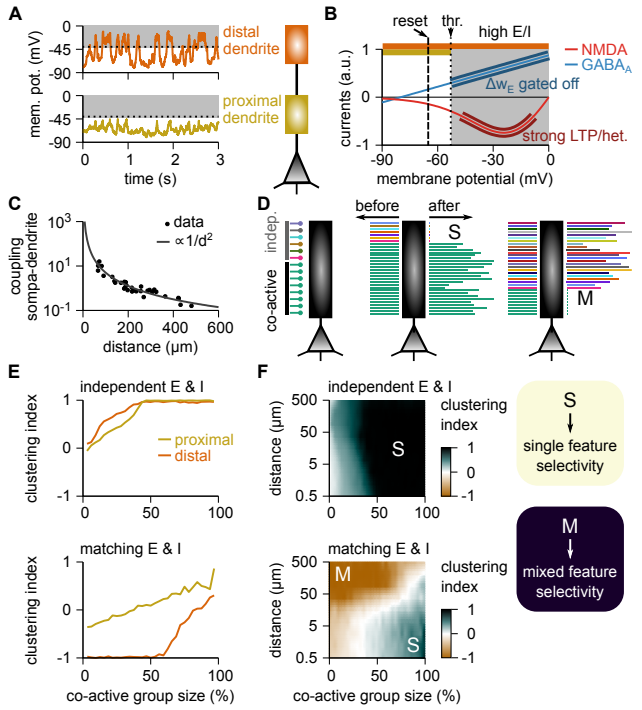

FIG. 3. Dendritic clustering. **A**, Membrane potential fluctuations at distal (top) and proximal (bottom) dendrites during ongoing stimulation. Dashed line shows the spiking threshold at the soma. **B**, NMDA (red) and $GABA_A$ (blue) currents as a function of membrane potential. Spiking threshold and reset are indicated by dotted and dashed lines, respectively. **C**, Coupling strength between soma and dendritic branch as a function of electrotonic distance fitted to experimental data[24]. **D**, *(Left)*, Schematic of the synaptic organisation onto a dendrite. Each line represents a synapse, with co-active synapses bearing the same colour. Examples of clustering of co-active (middle) or independent (right) synapses resulting in single feature selectivity (S) and mixed feature selectivity (M) at the level of the dendrite. Line length indicates synaptic weight in arbitrary units. **E**, Clustering index as a function to size of co-active input group for distal (orange) and proximal (yellow) dendrites with (top) or without (bottom) matching inhibitory inputs. Clustering index is equal to 1 (−1) when only co-active (independent) synapses survived and when 0 all synapses survived (Supp. M.). **F**, Same as E but showing dependency of distance between soma and dendritic branch.

with regard to the weights of incoming and outgoing synapses to find the neurons would most strongly affect the network (Supp. M.; Fig. 4E), together with baseline firing-rate of these neurons during background activity. When we delivered step-like stimuli to these neurons, their elevated firing rates maximally stimulated other neurons of the network, increasing or decreasing their responses based on the specific input pattern, and the network connectivity (Fig. 4F,G). We observed several types of responses, ranging from minimal deflections in firing rate to large transient responses, either during the delivery of the stimulus, or in response to its termination. To further quantify these responses, we calculated both the average and the ℓ_2-norm of the population (Fig. 4G). Both these measures confirmed that the network was in a regime of 'transient amplification' (Fig. 4G), i.e., a highly responsive state thought to underlie computation-through-population-dynamics[32]. What's more, the trajectory of the population dynamics in principle component space showed reliable network wide activity patterns (Fig. 4H) that could be used to control the activity of a readout network with two output units to draw digits (Fig. 4I).

In this paper we introduced a general framework to describe synaptic plasticity as a function of local pre- and postsynaptic interactions, including the modulatory effects of nearby synapses. We designed the excitatory and inhibitory plasticity rules according to experimental observations, such that the effect of neighbouring synapses gated, controlled and even flipped the direction of efficacy changes[4–12]. Importantly, excitatory and inhibitory plasticity strove towards different fixed points. They thus collaborated without mutual antagonism, in the process reproducing many relevant experimental results. In our model, inhibition played an important role to control excitatory plasticity, allowing for quick reorganisation of input patterns during periods of disinhibition, yet keeping memories stable when excitatory and inhibitory neurons were active. This control that inhibition exerted on excitatory plasticity also dictated whether co-active excitatory synapses clustered (or not) in a simplified dendritic model, providing a possible explanation for differing observations of dendritic input clustering in the recent literature[28,29]. Finally, our network results serve as a proof of principle that codependent plasticity can develop a stable, balanced network that amplify particular

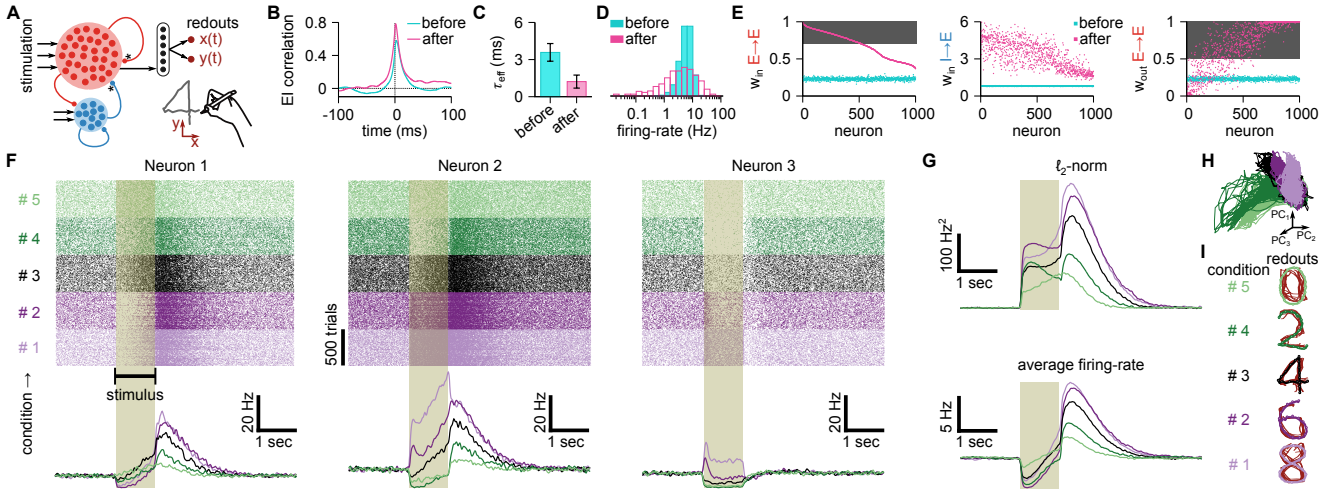

FIG. 4. Self-sustained activity and transient amplification in recurrent networks. A, Network of 1000 excitatory and 250 inhibitory neurons. Connections between excitatory neurons and from inhibitory to excitatory neurons are plastic (indicated by ∗). During learning external stimulation decreases over time until a state of self-sustained activity is reached. **B-E**, Summary of changes in excitatory neurons, before (cyan) and after (pink) a learning period of 60 minutes. **B**, Correlation between excitatory and inhibitory currents. **C**, Effective time constant, calculated as the membrane time constant divided by the sum of all conductances. **D**, Firing-rate distribution. **E**, Excitatory average input (left) and output (middle) weight, and inhibitory average weight (right) for all excitatory neurons, ordered by stronger input weights after learning. **F**, Raster plot (top) and mean firing-rate (bottom) of three excitatory neurons for five different stimulation patterns (conditions). **G**, Norm (top) and average firing-rate (bottom) of excitatory neurons for the five stimulation patterns in F. **H**, First three principal components of the activity of excitatory neurons from the recurrent network. Each line is the combination of 50 out of 500 trials to compensate for the high trial-to-trial variability. **I**, Output of two readout neurons trained to draw digits on a 2D-plane using the input from the excitatory neurons from the recurrent network (Supp. M.).

types of input, generating complex spatio-temporal patterns of activity. The networks that were constructed by codependent plasticity reproduced cortical activity patterns that were not trained for and could be used to emulate motor-like outputs for both average and single trial experiments[33,34]. Additional experimental work that can monitor multi-cell interactions by way of, e.g., all optical intervention *in vivo*[35,36] are necessary to help describe more complex synaptic interactions of multiple excitatory and inhibitory neuron types[37]. We are confident that codependence as a principle for plasticity will prove crucial in the face of increased complexity of these challenges.

Acknowledgements. We thank Chris Currin, Bill Podlaski, and the members of the Vogels group for fruitful discussions. This work was supported by a Research Project Grant by the Leverhulme Trust (RPG-2016-446; EJA), a Sir Henry Dale Fellowship by the Wellcome Trust and the Royal Society (WT100000; EJA, TPV), and a Wellcome Trust Senior Research Fellowship (214316/Z/18/Z; EJA, TPV).

References

[1] H. Markram, W. Gerstner, and P. J. Sjöström, Frontiers in Synaptic Neuroscience **3**, 4 (2011).
[2] M. Poo, M. Pignatelli, T. J. Ryan, S. Tonegawa, T. Bonhoeffer, K. C. Martin, A. Rudenko, L.-H. Tsai, R. W. Tsien, G. Fishell, C. Mullins, J. T. Gonçalves, M. Shtrahman, S. T. Johnston, F. H. Gage, Y. Dan, J. Long, G. Buzsáki, and C. Stevens, BMC Biology **14**, 40 (2016).
[3] G. Hennequin, E. J. Agnes, and T. P. Vogels, Annual Review of Neuroscience **40**, 557 (2017).
[4] J. A. D'amour and R. C. Froemke, Neuron **86**, 514 (2015).
[5] J. Mapelli, D. Gandolfi, A. Vilella, M. Zoli, and A. Bigiani, Proceedings of the National Academy of Sciences **113**, 9898 (2016).
[6] L. Wang and A. Maffei, Journal of Neuroscience **34**, 1083 (2014).
[7] V. Paille, E. Fino, K. Du, T. Morera-Herreras, S. Perez, J. H. Kotaleski, and L. Venance, Journal of Neuroscience **33**, 9353 (2013).
[8] P. J. Sjöström, G. G. Turrigiano, and S. B. Nelson, Neuron **32**, 1149 (2001).
[9] P. J. Sjöström and M. Häusser, Neuron **51**, 227 (2006).
[10] F. Brandalise, S. Carta, F. Helmchen, J. Lisman, and U. Gerber, Nature Communications **7**, 13480 (2016).
[11] D. Debanne, B. H. Gähwiler, and S. M. Thompson, Proceedings of the National Academy of Sciences **93**, 11225 (1996).
[12] C. D. Harvey and K. Svoboda, Nature **450**, 1195 (2007).
[13] G.-q. Bi and M.-m. Poo, Journal of Neuroscience **18**, 10464 (1998).
[14] M. Chistiakova and M. Volgushev, Experimental Brain Research **199**, 377 (2009).
[15] K. A. Wilmes, H. Sprekeler, and S. Schreiber, PLoS Computational Biology **12**, e1004768 (2016).
[16] M. A. Woodin, K. Ganguly, and M.-m. Poo, Neuron **39**, 807 (2003).
[17] F. Zenke, E. J. Agnes, and W. Gerstner, Nature Communications **6**, 6922 (2015).
[18] T. P. Vogels, H. Sprekeler, F. Zenke, C. Clopath, and W. Gerstner, Science **334**, 1569 (2011).
[19] J.-P. Pfister and W. Gerstner, Journal of Neuroscience **26**, 9673 (2006).
[20] C. Clopath, L. Büsing, E. Vasilaki, and W. Gerstner, Nature Neuroscience **13**, 344 (2010).
[21] A. Morrison, A. Aertsen, and M. Diesmann, Neural Computation **19**, 1437 (2007).
[22] T. Keck, G. B. Keller, R. I. Jacobsen, U. T. Eysel, T. Bonhoeffer, and M. Hübener, Neuron **80**, 327 (2013).
[23] R. C. Froemke, M. M. Merzenich, and C. E. Schreiner, Nature **450**, 425 (2007).
[24] A. T. Gulledge and G. J. Stuart, Journal of Neuroscience **23**, 11363 (2003).
[25] N. Takahashi, K. Kitamura, N. Matsuo, M. Mayford, M. Kano, N. Matsuki, and Y. Ikegaya, Science **335**, 353 (2012).
[26] D. E. Wilson, D. E. Whitney, B. Scholl, and D. Fitzpatrick, Nature Neuroscience **19**, 1003 (2016).
[27] H. Jia, N. L. Rochefort, X. Chen, and A. Konnerth, Nature **464**, 1307 (2010).
[28] T. Kleindienst, J. Winnubst, C. Roth-Alpermann, T. Bonhoeffer, and C. Lohmann, Neuron **72**, 1012 (2011).
[29] E. T. Kavalali, J. Klingauf, and R. W. Tsien, Proceedings of the National Academy of Sciences **96**, 12893 (1999).
[30] A. Destexhe, M. Rudolph, and D. Paré, Nature Reviews Neuroscience **4**, 739 (2003).
[31] K. B. Hengen, M. E. Lambo, S. D. Van Hooser, D. B. Katz, and G. G. Turrigiano, Neuron **80**, 335 (2013).
[32] S. Vyas, M. D. Golub, D. Sussillo, and K. V. Shenoy, Annual Review of Neuroscience **43**, 249 (2020).
[33] M. M. Churchland, M. Y. Byron, J. P. Cunningham, L. P. Sugrue, M. R. Cohen, G. S. Corrado, W. T. Newsome, A. M. Clark, P. Hosseini, B. B. Scott, D. C. Bradley, M. A. Smith, A. Kohn, J. A. Movshon, K. M. Armstrong, T. Moore, S. W. Chang, L. H. Snyder, S. G. Lisberger, N. J. Priebe, I. M. Finn, D. Ferster, S. I. Ryu, G. Santhanam, M. Sahani, and K. V. Shenoy, Nature Neuroscience **13**, 369 (2010).
[34] M. M. Churchland, J. P. Cunningham, M. T. Kaufman, J. D. Foster, P. Nuyujukian, S. I. Ryu, and K. V. Shenoy, Nature **487**, 51 (2012).
[35] A. M. Packer, L. E. Russell, H. W. P. Dalgleish, and M. Häusser, Nature Methods **12**, 140 (2015).
[36] M. B. Pardi, J. Vogenstahl, T. Dalmay, T. Spanò, D.-L. Pu, L. B. Naumann, F. Kretschmer, H. Sprekeler, and J. J. Letzkus, Science **370**, 844 (2020).
[37] X. Jiang, S. Shen, C. Cadwell, P. Berens, F. Sinz, A. Ecker, S. Patel, and A. Tolias, Science **350**, aac9462 (2015).

Supplementary material of
Interacting synapses stabilise both learning and neuronal dynamics in biological networks
Everton J. Agnes, and Tim P. Vogels

Neuron model

Point neuron. In the simulations with a postsynaptic neuron described by a single variable (point-neuron) we used a leaky integrate-and-fire (LIF) neuron with after-hyperpolarization (AHP) current and conductance-based synapses. The postsynaptic neuron's membrane potential, $u(t)$, evolved according to a first-order differential equation,

$$\begin{aligned}\tau_{\mathrm{m}}\frac{\mathrm{d}u(t)}{\mathrm{d}t} =& -[u(t)-u_{\mathrm{rest}}] - g_{\mathrm{AHP}}(t)[u(t)-E_{\mathrm{AHP}}] + RI_{\mathrm{ext}}(t)\\ &- g_{\mathrm{AMPA}}(t)[u(t)-E_{\mathrm{AMPA}}] - g_{\mathrm{GABA_A}}(t)[u(t)-E_{\mathrm{GABA_A}}]\\ &- g_{\mathrm{NMDA}}(t)H_{\mathrm{NMDA}}(u)[u(t)-E_{\mathrm{NMDA}}],\end{aligned} \tag{S1}$$

where τ_{m} is the membrane time constant ($\tau_{\mathrm{m}} = RC$; leak resistance times membrane capacitance), u_{rest} is the resting membrane potential, $g_{\mathrm{AHP}}(t)$ is the conductance of the AHP channel with reversal potential E_{AHP}, $I_{\mathrm{ext}}(t)$ is an external current used to mimic experimental protocols to induce excitatory plasticity, and $g_X(t)$ and E_X are the conductance and the reversal potential of the synaptic channel X, respectively, with $X = \{\mathrm{AMPA}, \mathrm{NMDA}, \mathrm{GABA_A}\}$. Excitatory NMDA channels were implemented with a nonlinear function of the membrane potential, caused by a Mg^{2+} block, whose effect was simulated via the function

$$H_{\mathrm{NMDA}}(u) = \left(1 + a_{\mathrm{NMDA}}\exp[b_{\mathrm{NMDA}}(u - E_{\mathrm{NMDA}})]\right)^{-1}, \tag{S2}$$

where a_{NMDA} and b_{NMDA} are parameters. The AHP conductance was modelled as

$$\frac{\mathrm{d}g_{\mathrm{AHP}}(t)}{\mathrm{d}t} = -\frac{g_{\mathrm{AHP}}(t)}{\tau_{\mathrm{AHP}}} + S_{\mathrm{post}}(t), \tag{S3}$$

where τ_{AHP} is the characteristic time of the AHP channel and $S_{\mathrm{post}}(t)$ is the spike train of the postsynaptic neuron,

$$S_{\mathrm{post}}(t) = \sum_k \delta(t - t^*_{k,\mathrm{post}}), \tag{S4}$$

where $t^*_{k,\mathrm{post}}$ is the time of the k*th* spike of the postsynaptic neuron, and $\delta(\cdot)$ is the Dirac's delta. The synaptic conductance was modelled as

$$\frac{\mathrm{d}g_X(t)}{\mathrm{d}t} = -\frac{g_X(t)}{\tau_X} + \sum_{j\in X} w_j(t)S_j(t), \tag{S5}$$

where τ_X is the characteristic time of the neuroreceptor X. The sum on the right-hand side of Eq. S5 corresponds to presynaptic spike trains weighted by the synaptic strength $w_j(t)$. The presynaptic spike train of neuron j was modelled as

$$S_j(t) = \sum_k \delta(t - t^*_{k,j}), \tag{S6}$$

where $t^*_{k,j}$ is the time of the k*th* spike of neuron j. The postsynaptic neuron elicited an action potential whenever the membrane potential crossed a spiking threshold from below. We simulated two types of threshold: fixed or adaptive.

Fixed spiking threshold. A fixed spiking threshold was implemented as a parameter, u_{th}. When the postsynaptic neuron's membrane potential crossed u_{th} from below, a spike was generated and the postsynaptic neuron's membrane potential was instantaneously reset to u_{reset}, and then clamped at this value for the duration of the refractory period, τ_{ref}. All simulations with a single postsynaptic neuron were implemented with a fixed spiking threshold.

Adapting spiking threshold. For the simulations of the recurrent network we used an adapting spiking threshold, $u_{\mathrm{th}}(t)$. When the postsynaptic neuron's membrane potential crossed $u_{\mathrm{th}}(t)$ from below, a spike was generated and the postsynaptic neuron's membrane potential was instantaneously reset to u_{reset} without any additional clamping of the membrane potential (the refractory period that results from the adapting threshold is calculated below). Upon spike, the adapting spiking threshold, $u_{\mathrm{th}}(t)$, was instantaneously set to u^*_{th}, decaying back to its baseline according to

$$\tau_{\mathrm{th}}\frac{\mathrm{d}u_{\mathrm{th}}(t)}{\mathrm{d}t} = -u_{\mathrm{th}}(t) + u^0_{\mathrm{th}}, \tag{S7}$$

where τ_{th} is the decaying time for the threshold variable, and u^0_{th} is the baseline for spike generation. The maximum depolarization of the membrane potential is linked to the reversal potential of NMDA, and thus the absolute refractory period can be calculated as

$$\tau_{\mathrm{ref}} = \tau_{\mathrm{m}}\ln\left(\frac{u^0_{\mathrm{th}} - u^*_{\mathrm{th}}}{u^0_{\mathrm{th}} - E_{\mathrm{NMDA}}}\right), \tag{S8}$$

which is the time the adapting threshold takes to decay to the same value as the reversal potential of the NMDA channels. Fig. S6 shows an example of two states that arise from the combination of an adapating threshold and NMDA currents.

Two-layer neuron. The two-layer neuron was simulated as a compartmental model with a spiking soma that receives input from N_B dendritic branches. The soma was modelled as a LIF neuron, and the dendrite as a leaky integrator (without generation of action potentials). Somatic membrane potential evolved according to

$$\tau_m \frac{du_{soma}(t)}{dt} = -[u_{soma}(t) - u_{rest}] - g_{AHP}(t)[u_{soma}(t) - E_{AHP}] - \sum_{i=1}^{N_B} J_i[u_{soma}(t) - u_i(t)]. \tag{S9}$$

The soma of the two-layer neuron was similar to the point neuron (Eq. S1), however, synaptic currents were injected on the dendritic tree, which interacted with the soma passively through the last term on the right-hand side of Eq. S9, J_i being the conductance that controls the current flow due to connection between the soma and the i*th* dendrite. In Eq. S9, $u_i(t)$ is the membrane potential of the dendritic branch i. When the somatic membrane potential, $u_{soma}(t)$, crossed the threshold, u_{th}, from below, the postsynaptic neuron generated an action potential, being instantaneously reset to u_{reset}, and then clamped at this value for the duration of the refractory period, τ_{ref}.

Dendritic compartments received presynaptic inputs, as well as a sink current from the soma. The membrane potential of the i*th* branch, $u_i(t)$, evolved according to the following differential equation,

$$\begin{aligned}\tau_m \frac{du_i(t)}{dt} = &- [u_i(t) - u_{rest}] - J_i[u_i(t) - u_{soma}(t)] \\ &- g_{AMPA,i}(t)[u_i(t) - E_{AMPA}] - g_{GABA_A,i}(t)[u_i(t) - E_{GABA_A}] \\ &- g_{NMDA,i}(t)H_{NMDA}(u_i)[u_i(t) - E_{NMDA}].\end{aligned} \tag{S10}$$

Spikes were not elicited in dendritic compartments, but due to the gating function $H_{NMDA}(u)$ and the absence of spiking threshold, voltage plateaus occurred naturally when multiple inputs arrived simultaneously on a compartment. We simulated two compartments with the same coupling with the soma, J_i: one whose synapses changed according to the codependent synaptic plasticity model, and one with fixed synapses that acted as a noise source.

Coupling strength as function of electrotonic distance. The crucial parameter introduced when including dendritic compartments was the coupling between soma and a dendritic compartment, J_i. Steady changes in membrane potential at the soma are attenuated at dendritic compartments, and this attenuation has been shown to decrease with distance. Without synaptic inputs, and steady membrane potential at both soma and dendritic compartments, Eqs. S9 and S10 are equal to zero, which results in

$$J_i = \frac{a_i}{1 - a_i}, \tag{S11}$$

where a_i is the passive dendritic attenuation of the dendritic compartment i,

$$a_i = \frac{\bar{u}_i - u_{rest}}{\bar{u}_{soma} - u_{rest}}, \tag{S12}$$

with $\bar{u}_{soma}$ being a constant steady-state held at the soma, and $\bar{u}_i$ being the resulting steady-state at the dendritic compartment i. The attenuation is a function of distance as follows,

$$a_i = f_a(d) = \frac{d_*^2}{d^2}, \tag{S13}$$

where d_* is a parameter we fitted from experimental data from Gulledge and Stuart[24] (Fig. 3C). We used this fitted parameter in Eq. S11 to approximate the distance to the soma in Fig. 3F according to the soma-dendrite coupling strength used in our simulations.

Codependent synaptic plasticity model

The codependent plasticity model is a function on both spike times and input currents. We first describe how synaptic currents are accounted and then how excitatory and inhibitory models were implemented. We defined a variable $E_i(t)$ to represent the process triggered by excitatory currents at the i*th* dendritic compartment. We considered NMDA currents, which reflect influx of calcium into the postsynaptic cell, as the trigger for biochemical processes that are represented by the state of $E_i(t)$. Its dynamics is described by

$$\tau_E \frac{dE_i(t)}{dt} = -E_i(t) - c_{NMDA,i}(t), \tag{S14}$$

where τ_E is the characteristic time of the excitatory trace and

$$c_{NMDA,i}(t) = g_{NMDA,i}(t)H_{NMDA}(u_i)[u_i(t) - E_{NMDA}] \tag{S15}$$

is the excitatory current flowing through NMDA channels. Inhibitory inputs contributed to the plasticity model through a variable $I_i(t)$. For the inhibitory trace, we used $GABA_A$ currents, which reflect influx of chloride, as the trigger of the process described by

$I_i(t)$. The inhibitory trace evolved as

$$\tau_{\mathrm{I}} \frac{\mathrm{d}I_i(t)}{\mathrm{d}t} = -I_i(t) + c_{\mathrm{GABA_A},i}(t), \tag{S16}$$

where τ_{I} is the characteristic time of the inhibitory trace, $c_{\mathrm{GABA_A},i}$ is the inhibitory current described as

$$c_{\mathrm{GABA_A},i}(t) = g_{\mathrm{GABA_A},i}(t)[u_i(t) - E_{\mathrm{GABA_A}}]. \tag{S17}$$

The index i is not taken into account for simulations with point-neurons. Notice that both $E_i(t)$ and $I_i(t)$ are in units of voltage because the conductance is unit-free in our neuron model implementation (Eq. S1).

Codependent excitatory synaptic plasticity. The codependent excitatory synaptic plasticity model is a spike-timing-dependent plasticity (STDP) model regulated by excitatory and inhibitory inputs through $E_i(t)$ and $I_i(t)$. The weight of the j*th* synapse onto the i*th* dendritic branch, $w_{ij}(t)$, changed according to

$$\frac{\mathrm{d}w_{ij}(t)}{\mathrm{d}t} = \phi_{\mathrm{E}}(E_i(t), I_i(t); S_j(t), S_{\mathrm{post}}(t)) = \left\{\left[A_{\mathrm{LTP}} x_j^+(t) E_i(t) - A_{\mathrm{het}} y_{\mathrm{post}}^E(t)(E_i(t))^2\right] S_{\mathrm{post}}(t) - A_{\mathrm{LTD}} y_{\mathrm{post}}^-(t) S_j(t) w_{ij}(t)\right\} \exp\left[-\frac{I_i(t)}{I^*}\right], \tag{S18}$$

where A_{LTP}, A_{het} and A_{LTD} are the learning rates of long-term potentiation, heterosynaptic plasticity and long-term depression, respectively. The additional parameter I^* defines the amount of control that inhibitory activity imposes onto excitatory synapses. Variables $S_{\mathrm{post}}(t)$ and $S_j(t)$ represent the postsynaptic and presynaptic spike trains, respectively, as described above for the neuron model (Eqs. S4 and S6). The trace of presynaptic spike train is represented by $x_j^+(t)$, and the traces of postsynaptic spike train (with different time scales) are represented by $y_{\mathrm{post}}^E(t)$ and $y_{\mathrm{post}}^-(t)$. They evolve in time according to

$$\frac{\mathrm{d}x_j^+(t)}{\mathrm{d}t} = -\frac{x_j^+(t)}{\tau_+} + S_j(t), \tag{S19}$$

$$\frac{\mathrm{d}y_{\mathrm{post}}^E(t)}{\mathrm{d}t} = -\frac{y_{\mathrm{post}}^E(t)}{\tau_{y\mathrm{post}}} + S_{\mathrm{post}}(t) \tag{S20}$$

and

$$\frac{\mathrm{d}y_{\mathrm{post}}^-(t)}{\mathrm{d}t} = -\frac{y_{\mathrm{post}}^-(t)}{\tau_-} + S_{\mathrm{post}}(t). \tag{S21}$$

For values of inhibitory trace larger than a threshold, $I_i(t) > I_{\mathrm{th}}$, we effectively blocked excitatory plasticity to mimic complete shunting of back-propagating action potentials[15]. We implemented maximum and minimum allowed values for excitatory weights, $w_{\mathrm{max}}^{\mathrm{E}} = 1$ and $w_{\mathrm{min}}^{\mathrm{E}} = 10^{-6}$, respectively.

Codependent inhibitory synaptic plasticity. Similar to the excitatory learning rule, the codependent inhibitory synaptic plasticity is a function of spike times and synaptic currents. The weight of the j*th* inhibitory synapse onto the i*th* dendritic compartment, $w_{ij}(t)$, changes over time according to a differential equation given by

$$\frac{\mathrm{d}w_{ij}(t)}{\mathrm{d}t} = \phi_{\mathrm{I}}(E_i(t), I_i(t); S_j(t), S_{\mathrm{post}}(t)) = \eta E_i(t)[E_i(t) - \alpha I_i(t)][y_{\mathrm{post}}(t) S_j(t) + x_j(t) S_{\mathrm{post}}(t)]. \tag{S22}$$

Parameters η and α control the learning-rate and the balance of excitatory and inhibitory currents, respectively. Variables $y_{\mathrm{post}}(t)$ and $x_j(t)$ are traces of pre and postsynaptic spike-trains, respectively, to create a symmetric STDP-like curve, with dynamics given by

$$\frac{\mathrm{d}y_{\mathrm{post}}(t)}{\mathrm{d}t} = -\frac{y_{\mathrm{post}}(t)}{\tau_{\mathrm{iSTDP}}} + S_{\mathrm{post}}(t) \tag{S23}$$

and

$$\frac{\mathrm{d}x_j(t)}{\mathrm{d}t} = -\frac{x_j(t)}{\tau_{\mathrm{iSTDP}}} + S_j(t). \tag{S24}$$

The STDP window is characterised by the time constant τ_{iSTDP}. We implemented maximum and minimum allowed values for inhibitory weights, $w_{\mathrm{max}}^{\mathrm{E}} = 7$ and $w_{\mathrm{min}}^{\mathrm{E}} = 10^{-6}$, respectively.

Experimental fit – Fig. 1D. We fitted two datasets with the codependent excitatory synaptic plasticity model to asses its dependency on voltage, i.e., membrane potential, and on the frequency of pre- and postsynaptic spikes. We used the same number of pre- and postsynaptic spikes for all our simulations (based on the original experiments). Postsynaptic spikes were induced by the injection of a current pulse, $I_{\mathrm{ext}}(t) = 3$ nA, for the duration of 2 ms.

For Fig. 1D, left, additional to the current injected for spike generation, we also injected a constant external current to depolarize the neuron's membrane potential. The protocol consisted in pre- and postsynaptic spikes with 10 millisecond interval, pre-before-post, firing at 50 Hz. The more depolarized the membrane potential, the bigger the effect of the NMDA currents, and therefore more LTP was induced.

The protocol for Fig. 1D, right, consisted on pre- and postsynaptic spikes with either +10 milliseconds (pre-before-post) or −10 milliseconds interval (post-before-pre) in varying firing-rates: 0.1, 10, 20, 40, and 50 Hz. The increase in presynaptic firing-rate caused a bigger accumulation in NMDA currents which increased LTP.

Fitting of both protocols was done with brute force parameter sweep on four parameters: A_{LTP}, A_{het}, A_{LTD}, and τ_{E}.

Stability. The codependent plasticity model has a rich dynamics that involves changes in synaptic weights due to pre and postsynaptic spike times, as well as synaptic weight and input currents. In this section we briefly analyse the fixed-points for input currents and synaptic weights for general conditions of inputs and outputs.

Considering separated dendritic compartments we can write the average change in weights (from Eq. S18, ignoring inhibitory inputs) as

$$\left\langle \frac{\mathrm{d}w_{ij}(t)}{\mathrm{d}t} \right\rangle_t = \left\langle S_{\text{post}}(t) \left[A_{\text{LTP}} x_j^+(t) E_i(t) - A_{\text{het}} y_{\text{post}}^E(t) (E_i(t))^2 \right] - A_{\text{LTD}} y_{\text{post}}^-(t) S_j(t) w_{ij}(t) \right\rangle_t \tag{S25}$$

$$= A_{\text{LTP}} \left\langle x_j^+(t) E_i(t) S_{\text{post}}(t) \right\rangle_t - A_{\text{het}} \left\langle S_{\text{post}}(t) y_{\text{post}}^E(t) (E_i(t))^2 \right\rangle_t - A_{\text{LTD}} \left\langle S_j(t) y_{\text{post}}^-(t) w_{ij}(t) \right\rangle_t \tag{S26}$$

$$= A_{\text{LTP}} \left\langle x_j^+(t) E_i(t) S_{\text{post}}(t) \right\rangle_t - A_{\text{het}} \left\langle S_{\text{post}}(t) \right\rangle_t \left\langle y_{\text{post}}^E(t) \right\rangle_t \left\langle (E_i(t))^2 \right\rangle_t - A_{\text{LTD}} \left\langle S_j(t) \right\rangle_t \left\langle y_{\text{post}}^-(t) \right\rangle_t \left\langle w_{ij}(t) \right\rangle_t, \tag{S27}$$

where $\langle \cdot \rangle_t$ is the average over a time window bigger than the timescale of the quantities involved. In Eq. S27 we take into consideration that presynaptic spike times are not influenced by postsynaptic activity, and thus the average of the products in the last term on the right-hand side of Eq. S26 is the equal to the product of the averages. Additionally, we assume no strong correlations between $E_i(t)$ and $S_{\text{post}}(t)$ due to the small fluctuations of the variable $E_i(t)$. Correlations between pre- and postsynaptic spikes govern the LTP term, and thus cannot be ignored. They also depend on the neuron model, and amount of inhibition a compartment is receiving.

We can conclude from Eq. S27 that the weights from silent presynaptic neurons will vanish due to the heterosynaptic term. In our model, these weights can only vanish in moments of disinhibition, when the inhibitory control over excitatory plasticity is minimum.

For our analysis, we consider that all neurons of the network have nearly stationary firing rates without strong fluctuations. Therefore, the spike trains can be rewritten as average firing rates,

$$\langle S_j(t) \rangle_t = \nu_j, \tag{S28}$$

and the traces from the spike trains become

$$\langle x_j^+(t) \rangle_t = \tau_+ \nu_j, \tag{S29}$$

where ν_j is the average firing rate of neuron j. The same is valid for the postsynaptic neuron's firing rate, as well as all other traces.

We first consider the outcome of the excitatory plasticity rule when LTD is not present, $A_{\text{LTD}} = 0$, which informs us on steady-state for excitatory currents as a competition between LTP and heterosynaptic plasticity only. In this case, the steady-state of the system is given by

$$\overline{E}_i \Big|_{A_{\text{LTD}}=0} \approx \frac{A_{\text{LTP}} \tau_+ \nu_j}{A_{\text{het}} \tau_{y\text{post}} \nu_{\text{post}}} = \overline{E}_i^{\text{max}}. \tag{S30}$$

This is also the maximum value for excitatory currents for when LTD is present, as LTD can only decrease synaptic weights. Notice that this fixed-point depends on both pre- and postsynaptic firing-rates, and thus an extra step in necessary to find the fixed-point. For a recurrent network, we can assume that $\nu_j = \nu_{\text{post}}$ and thus

$$\overline{E}_i^{\text{max,rec}} = \frac{A_{\text{LTP}} \tau_+}{A_{\text{het}} \tau_{y\text{post}}}. \tag{S31}$$

Notice that the maximum excitatory current onto a neuron embedded in a recurrent network is independent on firing-rate of pre- and postsynaptic neurons.

To have an idea of the contribution of LTD for the excitatory inputs, we aused a variant of the model in which LTD does not depend on the weight, $w_{ij}(t)$, and heterosynaptic plasticity does not depend on the postsynaptic trace, $y_{\text{post}}^E = 1$. We thus find that

$$\overline{E}_i = \frac{A_{\text{LTP}} \tau_+ \nu_j \pm \sqrt{\left(A_{\text{LTP}} \tau_+ \nu_j\right)^2 - 4 A_{\text{het}} A_{\text{LTD}} \tau_- \tau_{y\text{post}} \nu_j}}{2 A_{\text{het}} \tau_{y\text{post}}}. \tag{S32}$$

In Fig. 1E we simulated this version of the model with constant presynaptic firing-rate, ν_j, and plotted the theory as Eq. S32. To test the effect of input firing-rate and LTD with weight dependency, we simulated the protocol as in Fig. 1E, but with different levels of excitatory input, LTD, and inhibitory gating (Fig. S7). These simulations (Fig. S7 show that, although the input has an effect on the fixed-point of excitatory currents, this effect is minimal compared to the effect of the learning-rates.

Applying the same idea to the codependent inhibitory synaptic plasticity model, we get the following average dynamics for the inhibitory weight connecting presynaptic neuron j and the dendritic compartment i,

$$\left\langle \frac{\mathrm{d}w_{ij}(t)}{\mathrm{d}t} \right\rangle_t = \left\langle \eta E_i(t) [E_i(t) - \alpha I_i(t)] [y_{\text{post}}(t) S_j(t) + x_j(t) S_{\text{post}}(t)] \right\rangle_t \tag{S33}$$

$$\approx \eta \overline{E}_i \left[\overline{E}_i - \alpha \overline{I}_i \right] \left[2 \tau_{\text{iSTDP}} \nu_j \nu_{\text{post}} \right], \tag{S34}$$

where $\overline{I}_i = \langle I_i(t) \rangle_t$. From Eq. S34, we get the steady-state for the inhibitory learning rule, which results in the balance between

excitation and inhibition given by α,

$$\frac{\overline{E}_i}{\overline{I}_i} = \alpha. \tag{S35}$$

Inputs

Single output neuron (feedforward network). Presynaptic spike trains for single neurons were implemented as follows. A spike of neuron j occurs in a given timestep of duration Δt with probability $p_j(t)$ if there was no spike elicited during the refractory period beforehand, τ^E_{ref} for excitatory and τ^I_{ref} for inhibitory inputs, respectively, and zero otherwise. For a constant probability $p_j(t) = p_j$ the mean firing-rate, ν_j, is therefore

$$\nu_j = \frac{1}{\Delta t} p_j \left(1 - p_j\right)^{\tau^X_{ref}/\Delta t}. \tag{S36}$$

Different simulation paradigms (or tests) are defined by the input statistics, which are described below. When pathways are included, the probability of having a presynaptic spike changes over time to create correlations between different presynaptic inputs.

Constant firing-rate – Fig. 1E, Fig. 1F, and S7. When constant background firing-rate was simulated, presynaptic neurons fired action potentials with probability $p_j = 5 \times 10^{-5}$ for excitatory and $p_j = 10^{-4}$ for inhibitory neurons, resulting in $\nu_j \approx 4.88$ Hz for excitatory and $\nu_j \approx 9.51$ Hz for inhibitory neurons, considering that simulations were implemented with a time step $\Delta t = 0.1$ ms and that refractory periods were $\tau^E_{ref} = 5$ ms and $\tau^I_{ref} = 2.5$ ms.

Constant firing-rate – Fig. S1. To explore how neighbouring neurons would affect plasticity at a given synapse we simulated the same protocol from the frequency-dependency experiment[8] (Fig. 1D, right) with the addition of one excitatory and one inhibitory presynaptic neuron with different firing-rates (Fig. S1). These extra synapses were kept fixed during the simulation, and we tested different firing-rates (from 0 to 200 Hz). We simulated the codependent excitatory plasticity rule with (Fig. S1A) and without (Fig. S1B) inhibitory gating, and compared with spike-based[17,19] (Fig. S1C) and voltage-based[20] (Fig. S1D) learning rules (described below).

Variable firing-rate (pathways) for receptive-field plasticity – Fig. 2, Fig S2, and Fig. S3. For correlated inputs (defined as pathways), we generated spike trains using an inhomogeneous Poisson process. A pathway is defined as a group of 100 excitatory and 25 inhibitory afferents (spike trains of presynaptic neurons) with two components: a constant background firing-rate and a fluctuating firing-rate taken from an Ornstein-Uhlenbeck (OU) process as described below. The background firing-rate for all 800 excitatory and 200 inhibitory afferents was given by a probability of $p^{\text{bg}}_j = 2 \times 10^{-4}$ for excitatory and $p^{\text{bg}}_j = 4 \times 10^{-4}$ for inhibitory afferents, with respective background firing-rates of $\nu^{\text{bg}}_j \approx 1.98$ Hz and $\nu^{\text{bg}}_j \approx 3.96$ Hz for excitatory and inhibitory presynaptic neurons, respectively, considering a time step $\Delta t = 0.1$ ms and refractory periods of $\tau^E_{ref} = 5$ ms and $\tau^I_{ref} = 2.5$ ms.

The fluctuating firing-rate of the pathway μ was created from an OU process. We used an auxiliary, $y_\mu(t)$, variable that follows a stochastic dynamics given by

$$\frac{\mathrm{d}y_\mu(t)}{\mathrm{d}t} = -\frac{y_\mu(t)}{\tau_{\text{OU}}} + \xi_\mu(t), \tag{S37}$$

where τ_{OU} is the time-constant of the OU process, and $\xi_\mu(t)$ is a random variable drawn from a Gaussian distribution with zero-mean and unitary standard deviation. The fluctuating firing-rate was then defined as

$$\nu_\mu(t) = \nu^* \left[y_\mu(t)\right]_+, \tag{S38}$$

where $\nu^* = 250$ Hz is the amplitude of the fluctuations and $[\cdot]_+$ is a rectifying function. The probability of a spike generated because of the fluctuating firing-rate is thus $p^\mu_j(t) = \Delta t \nu_\mu(t)$. The probability of a presynaptic afferent j belonging to pathway μ due to both background and fluctuating firing-rate was given by

$$p_j(t) = p^\mu_j(t) + p^{\text{bg}}_j. \tag{S39}$$

In Fig. 2 we have two learning windows; in Fig. 2B to learn the initial receptive field profile, and Fig. 2C, to learn the new configuration of the receptive field profile. During both learning periods, we set the firing-rate of all inhibitory neurons to 40% of background firing-rate, and the inactive excitatory pathways to background firing-rate. The first learning period lasts 1.1 seconds and has the following sequence of activation of excitatory groups: 0.5 seconds for pathway number 6, followed by 0.2 seconds of pathway number 7, 0.2 seconds of pathway number 5, 0.1 seconds of pathway number 4, and finally 0.1 seconds of pathway number 8 (Fig. S2A). The second learning period lasts 0.2 seconds and we only activated pathway number 4 (Fig. S2B). Activation of a pathway consisted in increasing the firing-rate probability of $p_j = 0.01$, resulting in a firing-rate of $\nu_\mu \approx 60$ Hz.

Variable firing-rate (pathways) for dendritic clustering – Fig. 3 and Fig. S4. To explore the clustering effect on dendritic compartments we divided the input spikes in pathways to have co-active or independent presynaptic afferents. We used the same implementation as for the *Variable firing-rate (pathways) for receptive field plasticity* above, but we changed the number of afferents per group in both excitatory and inhibitory presynaptic inputs. A dendritic compartment received 32 excitatory and 16 inhibitory afferents. In Fig. 3E, Fig. 3F, and Fig. S4 we used two conditions: independent E & I, and matching E & I. In both cases, the number of excitatory afferents following the same fluctuating firing-rate was increased from 1 (0% co-active group size) to 32 (100% co-active group size), while the remaining excitatory afferents had independent fluctuating firing-rates. For independent excitatory and inhibitory inputs (independent E & I), all 16 inhibitory afferents followed independent fluctuating firing-rates. For matching excitatory and

inhibitory inputs (matching E & I), 8 inhibitory afferents followed the same fluctuations in firing-rate as the co-active excitatory group (of different sizes), while the other 8 inhibitory afferents were independent.

Recurrent network. The simulation with the recurrent network had two parts, the learning period with both excitatory and inhibitory plasticity active, and the recall period without plasticity mechanisms active.

Learning period. During the beginning of the learning period of $T = 10$ hours (Fig. S5) we kept the network receiving a minimum of external input to avoid inactivity. The implementation of presynaptic spike train was as follows. In the beginning of the simulation (first 1 hour of simulated time), each excitatory neuron of the network received a spike train from one external source with constant probability $p = 0.01$ (time step $\Delta t = 0.1$ ms) to mimic 100 presynaptic afferents firing at 1 Hz. We decreased the probability $p = 0.001$ for another 1 hour of simulated time, and then set it to zero. External inputs only affected AMPA conductances to keep the external influence on the network's dynamics minimal.

Recall period. To elicit transient amplification, we selected specific neurons to receive external input based on the resulted weight matrix and the neurons' baseline firing-rate. Before and after stimulation, no external input was implemented, meaning that the network was in a state of self-sustained activity. During the stimulation period, network neurons were stimulated with presynaptic spikes with a constant firing-rate with different amplitudes for each of the 5 conditions shown in Fig 4F-I. We ordered excitatory and inhibitory neurons according to their baseline firing-rate multiplied by total output weight (from maximum to minimum values), $\nu_j^{\mathrm{bg}} \sum_{i=1}^{N_{\mathrm{E}}} w_{ij}$ for excitatory and $\nu_j^{\mathrm{bg}} \sum_{i=1}^{N} w_{ij}$ for inhibitory neurons, where N_{E} is the total number of excitatory neurons, and N is the total number of neurons in the recurrent network. We assumed that the bigger the baseline firing-rate multiplied by the output weight, the bigger the neuron's influence on the rest of the network.

Considering the the order of maximal influence to minimal influence we used the following patterns of stimulation. For condition #1, external firing-rate was decreased from $p_i^{\mathrm{E}} = 0.1$ to $p_j^{\mathrm{E}} = 0$ for excitatory neurons, and followed the opposite order for inhibitory neurons. For condition #2, external firing-rate was increased from $p_i^{\mathrm{E}} = 0$ to $p_j^{\mathrm{E}} = 0.1$ for excitatory neurons, and followed the same order for inhibitory neurons. For condition #3, external firing-rate was decreased from $p_i^{\mathrm{E}} = 0.1$ to $p_j^{\mathrm{E}} = 0$ for excitatory neurons, and followed the same order for inhibitory neurons. For condition #4, external firing-rate was increased from $p_i^{\mathrm{E}} = 0$ to $p_j^{\mathrm{E}} = 0.1$ for excitatory neurons, and followed the opposite order for inhibitory neurons. For condition #5, external firing-rate was chosen randomly from a uniform distribution between $p_i^{\mathrm{E}} = 0$ and $p_j^{\mathrm{E}} = 0.1$ for excitatory neurons, and similarly for inhibitory neurons. Notice that the pattern of stimulation that activated excitatory and inactivated inhibitory neurons with large impact on the network (condition #1), amplification was the largest amongst the conditions, and when the pattern of stimulation was random (condition #5) the resulting network dynamics had minimum amplification (Fig. 4F,G).

Clustering index for dendritic dynamics - Fig. 3E,F.

We defined the clustering index as

$$c_{\mathrm{cluster}} = \frac{\langle w_{\text{co-active}} \rangle - \left\langle w_{\text{independent}} \right\rangle}{\langle w_{\text{co-active}} \rangle + \left\langle w_{\text{independent}} \right\rangle}, \tag{S40}$$

where $\langle w_{\text{co-active}} \rangle$ is the average of the weights from the co-active excitatory group, and $\langle w_{\text{co-active}} \rangle$ is the average of the weights from all independent groups after learning (see individual weight dynamics in Fig. S4). When $c_{\mathrm{cluster}} = 1$ the excitatory weights from the co-active group survived after learning, and independent ones vanished, while for $c_{\mathrm{cluster}} = -1$ the opposite happened. Both co-active and independent groups survived after learning when $c_{\mathrm{cluster}} \approx 0$.

Training an output to draw digits

We connected all excitatory neurons of our recurrent network to a two-layer network of nonlinear units. The second layer was connected to two nonlinear readouts that represented movement in the horizontal $x(t)$ and vertical $y(t)$ directions of a 2D plane. The dynamics of the i*th* unit of the first layer (total number of units $N_1 = 50$) was simulated as

$$h_i^{(1)}(t) = \tanh\left(\sum_{j=1}^{N_{\mathrm{E}}} W_{ij}^{(0)} \bar{r}_j(t)\right), \tag{S41}$$

where W_{ij} is the connection between neuron j from the network and the i*th* unit from the first layer and $\bar{r}_j(t)$ is the average firing-rate of neuron j (over 50 trials, see below). The dynamics of neuron j for an individual trial is given by

$$\frac{\mathrm{d}r_j(t)}{\mathrm{d}t} = -\frac{r_j(t)}{\tau_{\mathrm{r}}} + r_j^0(t) \tag{S42}$$

with

$$\frac{\mathrm{d}r_j^0(t)}{\mathrm{d}t} = -\frac{r_j^0(t)}{\tau_{\mathrm{r}}} + S_i(t). \tag{S43}$$

The firing-rate, $r_i(t)$, is the spike train of neuron i (Eq. S6) filtered twice (double exponential filter) with the time constant $\tau_{\mathrm{r}} = 10$ ms. As input to the first layer we used $\bar{r}_i(t)$ which is the average of $r_i(t)$ over 50 random trials out of 500 that were simulated. The second layer received input from the first layer, and the dynamics of the i*th* unit (total number of units $N_2 = 25$) of the second

layer was simulated as

$$h_i^{(2)}(t) = \tanh\left(\sum_{j=1}^{N_1} W_{ij}^{(1)} h_j^{(1)}(t)\right). \tag{S44}$$

The two readouts were simulated as,

$$\begin{cases} x(t) = \tanh\left(\sum_{i=1}^{N_2} W_{xi}^{(2)} h_i^{(2)}(t)\right) \\ y(t) = \tanh\left(\sum_{i=1}^{N_1} W_{yi}^{(2)} h_i^{(2)}(t)\right). \end{cases} \tag{S45}$$

The time-course of the simulation was divided into 35 bins of equal interval (ΔT = 30 ms), and the period after the stimulus onset was used to train the output weights to draw five digits: 0, 2, 4, 6, and 8, for the five different conditions from Fig. 4 that resulted from distinct patterns of stimulation. Each training epoch (single digit presentation) was simulated with the average firing-rate of 50 trials, randomly selected out of 500 to account for the large trial-to-trial variability of the spike patterns of each trial, mimicking a larger network in which groups of 50 neurons have a similar activity pattern. We used the same activity patterns fed to the two-layer network, $\bar{r}_i(t)$, to compute the principal components shown in Fig. 4H. All the weights were trained using gradient descent to minimise the square error between output and the drawing. Fig. 4I shows the average 2D trajectory for each digit in thick line, and 10 individual epochs in red lines. We did not perform any benchmark test as this is beyond the scope of this paper.

Comparison to other learning rules

We used spike-based learning rules to explore the balancing mechanisms of the codependent inhibitory synaptic plasticity rule (Fig. 1F). Additionally, we compared the excitatory codependent synaptic plasticity model with a spike- and a voltage-based learning rule when extra excitatory and inhibitory inputs are received by the postsynaptic neuron (Fig. S1).

Spike-based plasticity rules. We implemented spike-based learning rules that have been developed to impose a set-point for postsynaptic neurons. In Fig. 1F, left, we combined excitatory and inhibitory spike-based plasticity rules to show how they can destructively compete when their firing-rate set-points do not match. In Fig. 1F, right, we combined an excitatory spike-based plasticity rule with the codependent inhibitory synaptic plasticity rule to show how the competition is not present when the plasticity rules dynamics follow fixed-points for different quantities – here ESP imposes a firing-rate set-point while ISP imposes an input currents set-point. We also compared the spike-based excitatory plasticity rule to compare to the codependent excitatory plasticity rule for the same protocol in Fig. 1D, right, but adding activity of an excitatory and an inhibitory neuron with different firing-rates (Fig. S1C).

Spike-based excitatory plasticity rule. The excitatory plasticity rule was based on Pfister and Gerstner [19] and Zenke *et al.* [17]. We used a modified version from Zenke *et al.* [17] to create a stable-fixed point for the postsynaptic firing-rate. The weight from neuron j to neuron i changes according to

$$\frac{\mathrm{d}w_{ij}(t)}{\mathrm{d}t} = A_{\mathrm{pre}} S_j(t) + A_{\mathrm{LTP}} x_j^+(t) y_i(t) S_i(t) - A_{\mathrm{LTD}} x_i^-(t) S_j(t), \tag{S46}$$

where A_{pre}, A_{LTP}, and A_{LTD}, are the learning rates for the neurotransmitter induced plasticity, long-term potentiation, and long-term depression, respectively. The spike train of pre- and postsynaptic neurons, $S_j(t)$ and $S_i(t)$, respectively, are defined by Eq. S6 and Eq. S4. The traces $x_j^+(t)$, $y_i(t)$, and $x_i^-(t)$ followed the same dynamics described in Eq. S19, with time constants τ_+, τ_y, and τ_-, respectively. The learning rule described by Eq. S46 has a stable fixed-point for low postsynaptic firing-rate. The stable firing-rate set point was given by

$$\nu_0^{\mathrm{E}} = \frac{1}{2A_{\mathrm{LTP}}\tau_+\tau_y}\left(A_{\mathrm{LTD}}\tau_- - \sqrt{A_{\mathrm{LTD}}^2\tau_-^2 - 4A_{\mathrm{pre}}A_{\mathrm{LTP}}\tau_+\tau_y}\right). \tag{S47}$$

To change the firing-rate set-point during the simulation in Fig. 1F, we changed A_{pre}, keeping all the other parameters fixed.

Spike-based inhibitory plasticity rule. The spike-based inhibitory plasticity rule was based on Vogels *et al.* [18]. This inhibitory plasticity rule follows a Hebbian-like shape that imposes a postsynaptic firing-rate set-point by balancing excitation and inhibition. An inhibitory weight from neuron j to neuron i evolved as

$$\frac{\mathrm{d}w_{ij}(t)}{\mathrm{d}t} = \eta\left\{x_j(t)S_i(t) + [x_i(t) - \alpha]\, S_j(t)\right\}, \tag{S48}$$

where η is the learning rate, $x_j(t)$ and $x_i(t)$ are traces of pre- and postsynaptic spike trains, respectively, and they evolve with the same time constant τ_{iSTDP}. This learning rule is known to result in a stable firing-rate set-point for postsynaptic neurons given by

$$\nu_0^{\mathrm{I}} = \frac{\alpha}{2\tau_{\mathrm{iSTDP}}}. \tag{S49}$$

Voltage-based excitatory plasticity rule. We also compared the codependent excitatory synaptic plasticity model with a voltage-based model for a frequency dependent protocol[8] when additional presynaptic activity is included (Fig. S1D). The excitatory weight of the connection from neuron j to neuron i changed according to

$$\frac{\mathrm{d}w_{ij}(t)}{\mathrm{d}t} = A_{\mathrm{LTP}} x_j(t)\,[u_i(t) - \theta_+]_+ \left[\overline{u^+}_i(t) - \theta_-\right]_+ - A_{\mathrm{LTD}}\left[\overline{u^-}_i(t) - \theta_-\right]_+ S_j(t), \tag{S50}$$

where A_{LTP} and A_{LTD} are the learning rates for LTP and LTD, respectively, $x_j(t)$ is the trace of the presynaptic spike train, θ_+ is the

voltage threshold for LTP, θ_- is the voltage threshold (for the voltage low pass-filter) for LTP and LTD. The trace of the presynaptic spike train is given by

$$\frac{\mathrm{d}x_j(t)}{\mathrm{d}t} = -\frac{x_j(t)}{\tau_x} + S_j(t), \tag{S51}$$

where τ_x is the time constant for the trace. The voltage-based learning rule depends on the low-pass filter of the membrane potential, which creates a dependency on the recent history of membrane potential. There are two low-pass filters in the voltage-based model: one for LTP ($\overline{u^+}_i$) and one for LTD ($\overline{u^-}_i$) with dynamics given by

$$\tau_+ \frac{\mathrm{d}\overline{u^+}_i(t)}{\mathrm{d}t} = -\overline{u^+}_i(t) + u_i(t) \tag{S52}$$

and

$$\tau_- \frac{\mathrm{d}\overline{u^-}_i(t)}{\mathrm{d}t} = -\overline{u^-}_i(t) + u_i(t), \tag{S53}$$

where τ_+ and τ_- are the time constants for the voltage low-pass filters for LTP and LTD, respectively.

To account for the plasticity inducing effects of the action potential, we modified the LIF neuron model so that it had a short depolarized period corresponding to the action potential. Following the implementation from the subsection *Point neuron - Fixed spiking threshold*, when the membrane potential crossed the threshold, u_{th} from below, the membrane potential was instantaneously set to $u_{AP} = 30$ mV, and it was then clamped at this voltage for the duration of the action potential $\tau_{\mathrm{AP}} = 2$ ms. After the duration of the action potential, the membrane potential was instantaneously reset to $u_{\mathrm{reset}}^{\mathrm{volt}} = -52$ mV.

Parameters

Parameter	Symbol	Value	Figs.
Membrane time constant	τ_m	30 ms	1, 2, 3, 4, S1, S3, S4, S5, S6, & S7
Membrane resistance	R	100 MΩ	1D & S1
Membrane capacitance	C	30 nF	not explicitly used
Resting potential	u_{rest}	−65 mV	1, 2, 3, 4, S1, S3, S4, S5, S6, & S7
AHP reversal potential	E_{AHP}	−80 mV	1, 2, 3, 4, S1, S3, S4, S5, S6, & S7
AMPA reversal potential	E_{AMPA}	0 mV	1, 2, 3, 4, S1, S3, S4, S5, S6, & S7
$GABA_A$ reversal potential	E_{GABA_A}	−80 mV	1, 2, 3, 4, S1, S3, S4, S5, S6, & S7
NMDA reversal potential	E_{NMDA}	0 mV	1, 2, 3, 4, S1, S3, S4, S5, S6, & S7
AHP time constant	τ_{AHP}	100 ms	1, 2, 3, 4, S1, S3, S4, S5, S6, & S7
AMPA time constant	τ_{AMPA}	5 ms	1, 2, 3, 4, S1, S3, S4, S5, S6, & S7
$GABA_A$ time constant	τ_{GABAA}	10 ms	1, 2, 3, 4, S1, S3, S4, S5, S6, & S7
NMDA time constant	τ_{NMDA}	150 ms	1, 2, 3, 4, S1, S3, S4, S5, S6, & S7
NMDA parameter 1	a_{NMDA}	0.15	1, 2, 3, 4, S1, S3, S4, S5, S6, & S7
NMDA parameter 2	b_{NMDA}	-0.08 mV^{-1}	1, 2, 3, 4, S1, S3, S4, S5, S6, & S7
Fixed spiking threshold	u_{th}	−50 mV	1, 2, 3, S1, S3, S4 & S7
Spiking threshold reset	u^*_{th}	10 mV	1, 2, 3, 4, S1, S3, S4, S5, S6, & S7
Spiking threshold steady-state	u^0_{th}	−50 mV	4, S5, & S6
Spiking threshold time constant for excitatory neurons	τ_{th}	10 ms	4, S5, & S6
Spiking threshold time constant for inhibitory neurons	τ_{th}	5 ms	4, S5, & S6
Reset potential	u_{reset}	−60 mV	1, 2, 3, 4, S1, S3, S4, S5, S6, & S7
Refractory period (when spiking threshold is fixed)	τ_{ref}	5 ms	1, 2, 3, 4, S1, S3, S4, S5, S6, & S7
Voltage attenuation between soma and dendritic compartment	d_*	49084.1 μm	3 & S4
Simulation time step	Δt	0.1 ms	1, 2, 3, 4, S1, S3, S4, S5, S6, & S7

TABLE S1. Simulation parameters for the leaky integrate-and-fire neuron.

Parameter	Symbol	Value	Figs.
Excitatory current filter time constant	τ_E	10 ms	1D (left)
Excitatory current filter time constant	τ_E	50 ms	1D (right)
Excitatory current filter time constant	τ_E	100 ms	1E & 1F
Inhibitory current filter time constant	τ_I	100 ms	1F
LTP learning rate for codependent ESP	A_{LTP}	10×10^{-5} mV^{-1}	1D (left)
LTP learning rate for codependent ESP	A_{LTP}	2.5×10^{-3} mV^{-1}	1D (right)
LTP learning rate for codependent ESP	A_{LTP}	10^{-5} mV^{-1}	1E
Heterosynaptic plasticity learning rate for codependent ESP	A_{het}	10^{-6} mV^{-2}	1D (left)
Heterosynaptic plasticity learning rate for codependent ESP	A_{het}	10^{-5} mV^{-2}	1D (right)
Heterosynaptic plasticity learning rate for codependent ESP	A_{het}	variable ($\times 10^8$)	1E
LTD learning rate for codependent ESP	A_{LTD}	10^{-2}	1D (left)
LTD learning rate for codependent ESP	A_{LTD}	1.2×20^{-2}	1D (right)
LTD learning rate for codependent ESP	A_{LTD}	4×10^{-4}	1E
Presynaptic trace time constant for codependent ESP	τ_+	16.8 ms	1D & 1E
Postsynaptic trace time constant for codependent ESP	τ_{ypost}	100 ms	1D
Postsynaptic trace time constant for codependent ESP	τ_{ypost}	N/A	1E
Postsynaptic trace time constant for codependent ESP	τ_-	33.7 ms	1D & 1E
Inhibitory plasticity learning rate	η	10^{-8} mV^{-2}	1F (right)
Inhibitory balance set-point	α	15	1F (right)
Pre- and postsynaptic traces time constant for codependent ISP	τ_{iSTDP}	20 ms	1F (right)

TABLE S2. Simulation parameters for codependent synaptic plasticity model in Fig. 1.

Parameter	Symbol	Value	Figs.
Neurotransmitter induced plasticity learning rate for spike-based ESP	A_{pre}	$\{9.4, 15, 9.4, 5\} \times 10^{-3}$	1F
LTP learning rate for spike-based ESP	A_{LTP}	10^{-3}	1F
LTD learning rate for spike-based ESP	A_{LTD}	4.5×10^{-2}	1F
Presynaptic trace time constant for spike-based ESP	τ_{+}	16.8 ms	1F
Postsynaptic trace time constant for spike-based ESP	τ_{y}	100 ms	1F
Postsynaptic trace time constant for spike-based ESP	τ_{-}	33.7 ms	1F
Spike-based inhibitory plasticity learning rate	η	10^{-3}	1F (left)
Spike-based inhibitory plasticity LTD	α	0.228	1F (left)
Pre- and postsynaptic traces time constant for codependent ISP	τ_{iSTDP}	20 ms	1F (left)

TABLE S3. Simulation parameters for spike-based synaptic plasticity models in Fig. 1.

Parameter	Symbol	Value	Figs.
Excitatory current filter time constant	τ_{E}	10 ms	2 & S3
Inhibitory current filter time constant	τ_{I}	100 ms	2 & S3
LTP learning rate for codependent ESP	A_{LTP}	5×10^{-4} mV^{-1}	2 & S3
Heterosynaptic plasticity learning rate for codependent ESP	A_{het}	10^{-8} mV^{-2}	2 & S3
LTD learning rate for codependent ESP	A_{LTD}	0.5	2 & S3
Inhibitory gating term for codependent ESP	I^{*}	60 mV	2
Inhibitory gating term for codependent ESP	I^{*}	600 mV	S3
Inhibitory threshold for codependent ESP	I_{th}	200 mV	2
Inhibitory threshold for codependent ESP	I_{th}	2000 mV	S3
Presynaptic trace time constant for codependent ESP	τ_{+}	16.8 ms	2 & S3
Postsynaptic trace time constant for codependent ESP	$\tau_{y\text{post}}$	100 ms	2 & S3
Postsynaptic trace time constant for codependent ESP	τ_{-}	33.7 ms	2 & S3
Inhibitory plasticity learning rate	η	10^{-9} mV^{-2}	2 & S3
Inhibitory balance set-point	α	0.94	2 & S3
Pre- and postsynaptic traces time constant for codependent ISP	τ_{iSTDP}	20 ms	2 & S3

TABLE S4. Simulation parameters for codependent synaptic plasticity model in Fig. 2 and Fig. S3.

Parameter	Symbol	Value	Figs.
Excitatory current filter time constant	τ_{E}	10 ms	3 & S4
Inhibitory current filter time constant	τ_{I}	100 ms	3 & S4
LTP learning rate for codependent ESP	A_{LTP}	3×10^{-5} mV^{-1}	3 & S4
Heterosynaptic plasticity learning rate for codependent ESP	A_{het}	6×10^{-9} mV^{-2}	3 & S4
LTD learning rate for codependent ESP	A_{LTD}	1.5×10^{-3}	3 & S4
Inhibitory gating term for codependent ESP	I^{*}	50 mV	3 & S4
Inhibitory threshold for codependent ESP	I_{th}	N/A	3 & S4
Presynaptic trace time constant for codependent ESP	τ_{+}	16.8 ms	3 & S4
Postsynaptic trace time constant for codependent ESP	$\tau_{y\text{post}}$	100 ms	3 & S4
Postsynaptic trace time constant for codependent ESP	τ_{-}	33.7 ms	3 & S4
Inhibitory plasticity learning rate	η	10^{-7} mV^{-2}	3 & S4
Inhibitory balance set-point	α	1.75	3 & S4
Pre- and postsynaptic traces time constant for codependent ISP	τ_{iSTDP}	20 ms	3 & S4

TABLE S5. Simulation parameters for codependent synaptic plasticity model in Fig. 3 and Fig. S4.

Parameter	Symbol	Value	Figs.
Excitatory current filter time constant	τ_{E}	10 ms	4 & S5
Inhibitory current filter time constant	τ_{I}	100 ms	4 & S5
LTP learning rate for codependent ESP	A_{LTP}	3×10^{-4} mV^{-1}	4 & S5
Heterosynaptic plasticity learning rate for codependent ESP	A_{het}	1.5×10^{-8} mV^{-2}	4 & S5
LTD learning rate for codependent ESP	A_{LTD}	3×10^{-5}	4 & S5
Inhibitory gating term for codependent ESP	I^*	200 mV	4 & S5
Presynaptic trace time constant for codependent ESP	τ_+	16.8 ms	4 & S5
Postsynaptic trace time constant for codependent ESP	$\tau_{y\mathrm{post}}$	100 ms	4 & S5
Postsynaptic trace time constant for codependent ESP	τ_-	33.7 ms	4 & S5
Inhibitory plasticity learning rate	η	10^{-8} mV^{-2}	4 & S5
Inhibitory balance set-point	α	1.2	4 & S5
Pre- and postsynaptic traces time constant for codependent ISP	τ_{iSTDP}	20 ms	4 & S5

TABLE S6. Simulation parameters for codependent synaptic plasticity model in Fig. 4 and Fig. S5.

Parameter	Symbol	Value	Figs.
Excitatory current filter time constant	τ_{E}	50 ms	S1A,B
Inhibitory current filter time constant	τ_{I}	500 ms	S1A,B
LTP learning rate for codependent ESP	A_{LTP}	2.5×10^{-3} mV^{-1}	S1A,B
Heterosynaptic plasticity learning rate for codependent ESP	A_{het}	10^{-5} mV^{-2}	S1A,B
LTD learning rate for codependent ESP	A_{LTD}	1.2×10^{-2}	S1A,B
Inhibitory gating term for codependent ESP	I^*	10 mV	S1A
Inhibitory gating term for codependent ESP	I^*	N/A	S1B
Inhibitory threshold for codependent ESP	I_{th}	N/A	S1A,B
Presynaptic trace time constant for codependent ESP	τ_+	16.8 ms	S1A,B
Postsynaptic trace time constant for codependent ESP	$\tau_{y\mathrm{post}}$	100 ms	S1A,B
Postsynaptic trace time constant for codependent ESP	τ_-	33.7 ms	S1A,B

TABLE S7. Simulation parameters for codependent synaptic plasticity model in Fig. S1A,B.

Parameter	Symbol	Value	Figs.
Neurotransmitter induced plasticity learning rate for spike-based ESP	A_{pre}	0	S1C
LTP learning rate for spike-based ESP	A_{LTP}	10^{-3}	S1C
LTD learning rate for spike-based ESP	A_{LTD}	4.5×10^{-2}	S1C
Presynaptic trace time constant for spike-based ESP	τ_+	16.8 ms	S1C
Postsynaptic trace time constant for spike-based ESP	τ_y	100 ms	S1C
Postsynaptic trace time constant for spike-based ESP	τ_-	33.7 ms	S1C
LTP learning rate for voltage-based ESP	A_{LTP}	10^{-6} mV^{-2}ms^{-1}	S1D
LTD learning rate for voltage-based ESP	A_{LTD}	6×10^{-5} mV^{-1}	S1D
Voltage threshold for LTD	θ_-	−52 mV	S1D
Voltage threshold for LTP	θ_+	−55 mV	S1D
Presynaptic trace time constant for spike-based ESP	τ_x	15 ms	S1D
Voltage trace time constant for voltage-based ESP variable $\overline{u^-}_i$	τ_-	10 ms	S1D
Voltage trace time constant for voltage-based ESP variable $\overline{u^+}_i$	τ_+	150 ms	S1D

TABLE S8. Simulation parameters for spike- and voltage-based synaptic plasticity models in Fig. S1C,D.

Parameter	Symbol	Value	Figs.
Excitatory current filter time constant	τ_E	10 ms	S7
Inhibitory current filter time constant	τ_I	N/A	S7A,B
Inhibitory current filter time constant	τ_I	100 ms	S7C,D
LTP learning rate for codependent ESP	A_{LTP}	10^{-5} mV^{-1}	S7
Heterosynaptic plasticity learning rate for codependent ESP	A_{het}	variable	S7
LTD learning rate for codependent ESP	A_{LTD}	$\times 10^{-3}$	S7A,C
LTD learning rate for codependent ESP	A_{LTD}	$\times 10^{-2}$	S7B,D
Inhibitory gating term for codependent ESP	I^*	60 mV	S7A,B
Inhibitory gating term for codependent ESP	I^*	N/A	S7C,D
Inhibitory threshold for codependent ESP	I_{th}	N/A	S7
Presynaptic trace time constant for codependent ESP	τ_+	16.8 ms	S7
Postsynaptic trace time constant for codependent ESP	τ_{ypost}	100 ms	S7
Postsynaptic trace time constant for codependent ESP	τ_-	33.7 ms	S7

TABLE S9. Simulation parameters for codependent synaptic plasticity model in Fig. S7.

Supplementary figures of

Interacting synapses stabilise both learning and neuronal dynamics in biological networks

Everton J. Agnes and Tim P. Vogels

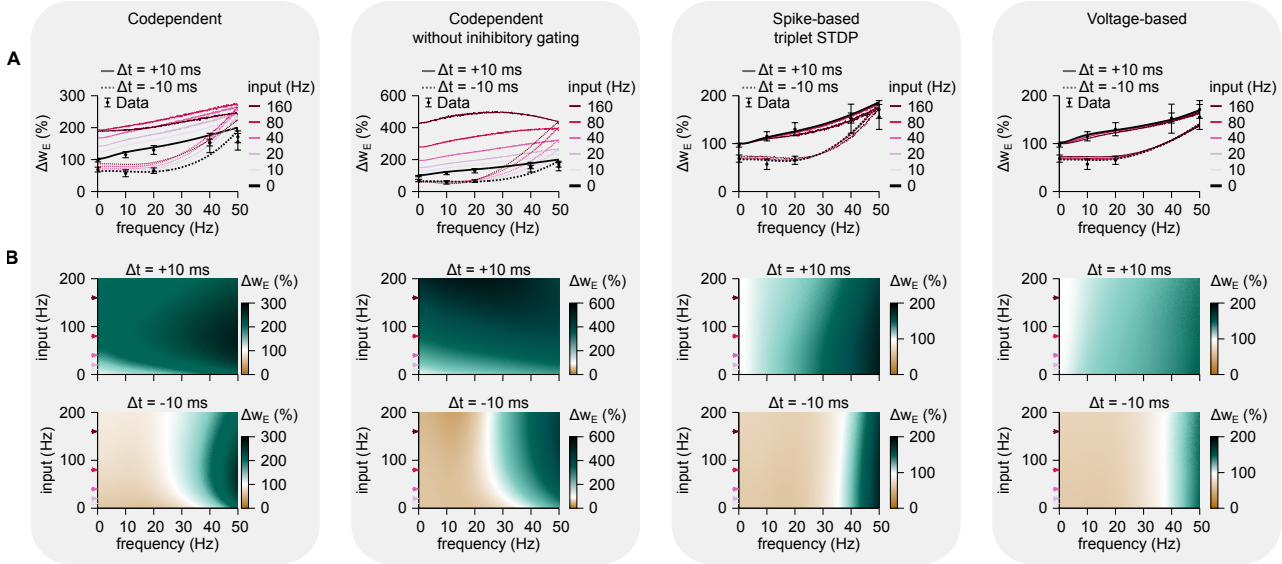

FIG. S1. Comparison between synaptic plasticity models. A, Plasticity inducing protocol with pairs of pre-before-post ($\Delta t = +10$ ms) and post-before-pre ($\Delta t = -10$ ms) for varying spiking frequencies, and different firing-rates of neighbouring excitatory and inhibitory afferents (different colours). Plot shows changes in synaptic weight of a single connection while the other two (excitatory and inhibitory) are kept fixed. Excitatory and inhibitory weight of neighbouring synapses were chosen to keep the initial (before plasticity) excitatory and inhibitory currents balanced, and thus same average membrane potential for the same input frequency. Experimental data from Sjöström *et al.* [8]; spike-based triplet spike timing-dependent-plasticity model from Pfister and Gerstner [19], and voltage-based plasticity model from Clopath *et al.* [20]. **B**, Weight changes as a function of input frequency (from neighbouring excitatory and inhibitory synapses; y-axis), and frequency of pairs of spikes (x-axis).

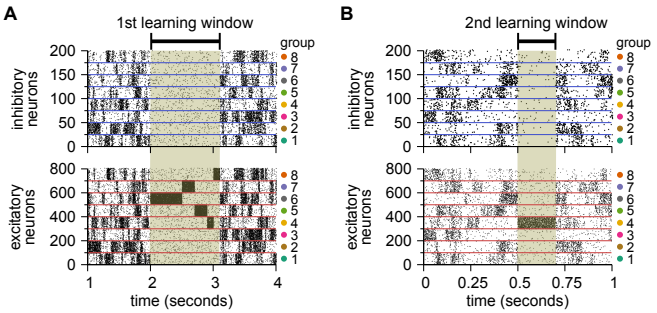

FIG. S2. Raster plot of inhibitory (top) and excitatory (bottom) neurons used in the receptive field plasticity simulation (Fig. 2). A, Input spike patterns before ($t < 2$ s), during ($2 < t < 3.1$ s), and after ($t > 3.1$ s) learning the initial receptive field profile (Fig. 2B). **B**, Sequence of input spikes for the modification of the initial receptive field profile, before ($t < 0.5$ s), during ($0.5 < t < 0.6$ s), and after ($t > 0.6$ s) the learning window.

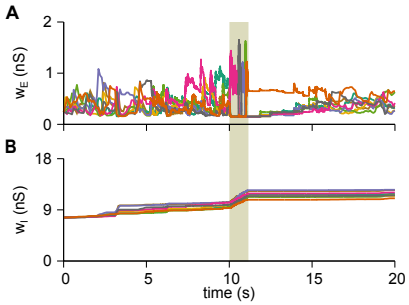

FIG. S3. Evolution of synaptic weights for receptive field plasticity (same input pattern as in Fig. 2B) when inhibitory gating is weak. A, Evolution of excitatory weights, colour coded as in Fig. 2. Note that the receptive field profile is not maintained without inhibitory gate. **B**, Inhibitory weights colour coded as in Fig. 2. Learning window represented by the shaded area (*).

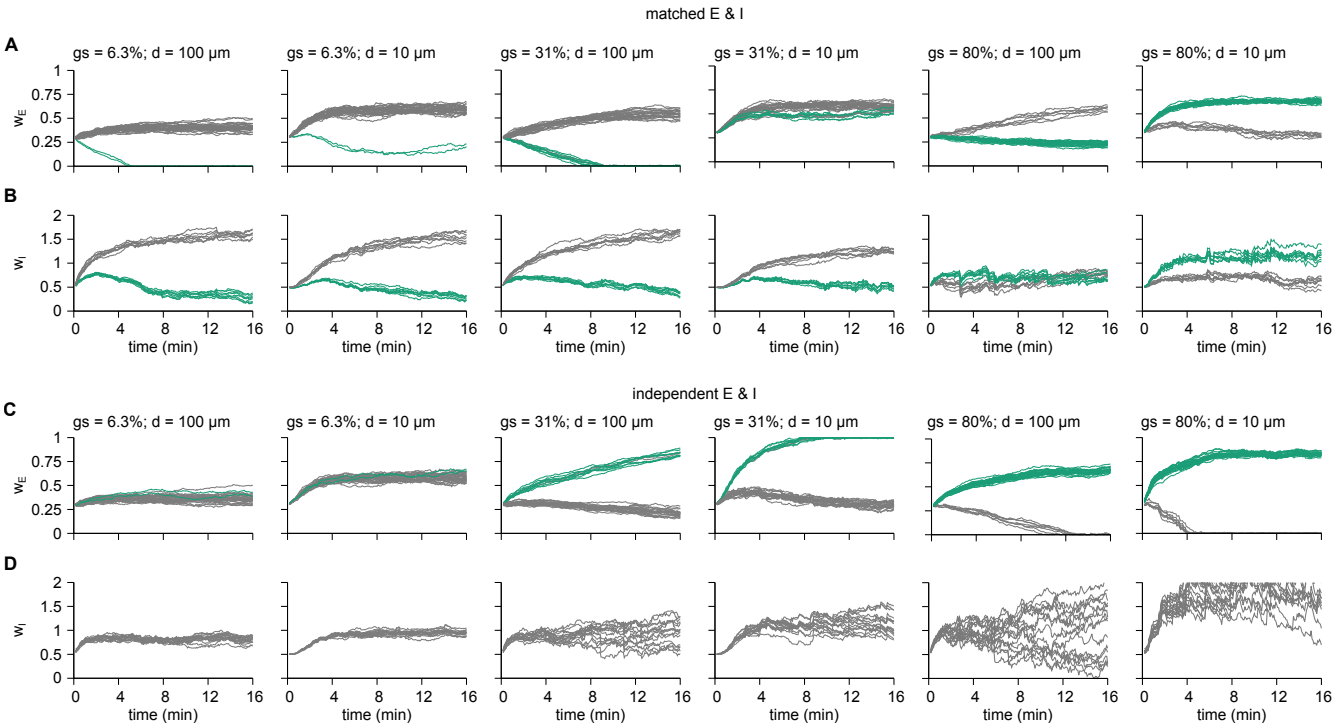

FIG. S4. Evolution of synaptic weights connected to dendritic compartments for matched and independent E & I. A, Weights of co-active (green) and uncorrelated (gray) excitatory inputs with size of co-active excitatory group and distance of dendritic compartment from the soma indicated by gs and d, respectively. **B**, Weights of co-active (green; same activity pattern as co-active excitatory group) and uncorrelated (gray) inhibitory inputs. Size of co-active inhibitory group was kept fixed at half of the inhibitory population. **C**, Same as panel A, but when inhibitory inputs are independent of excitatory ones. **D**, Same as in panel B, but with no correlation between excitatory and inhibitory inputs.

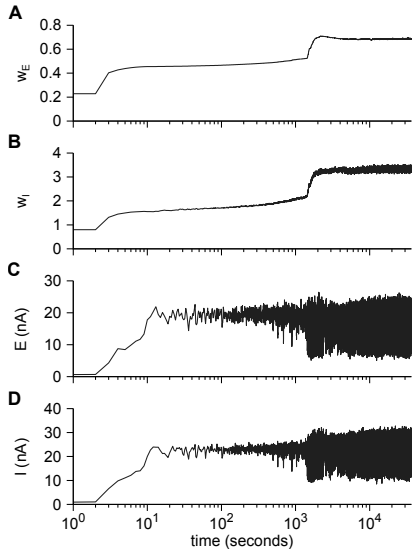

FIG. S5. Learning period for the recurrent network (Fig. 4). A, Average of recurrent excitatory weights. **B**, Average of inhibitory weights onto excitatory neurons. **C**, Average of excitatory currents onto excitatory neurons. **D**, Average of inhibitory currents onto excitatory neurons.

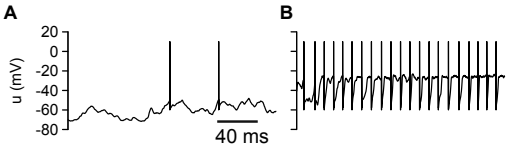

FIG. S6. Low and high firing-rate states for neurons with adapting spiking threshold and NMDA currents. A, Membrane potential of a neuron in a hyperpolarised state with low firing-rate. **B**, Membrane potential of a neuron in a depolarised state with high firing-rate.

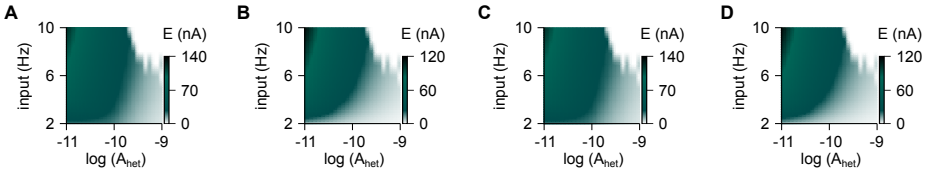

FIG. S7. Final excitatory currents of a postsynaptic neuron as a function of heterosynaptic plasticity and input firing-rate. A, Simulation with weak LTD and weak inhibitory gating. **B**, Simulation with strong LTD and weak inhibitory gating. **C**, Simulation with weak LTD and strong inhibitory gating. **D**, Simulation with strong LTD and strong inhibitory gating. High heterosynaptic learning-rates caused vanishing of weights when inputs have higher firing-rate.